MODELLING INTERNAL FLOW AND PRIMARY ATOMIZATION IN A SIMPLEX PRESSURE-SWIRL ATOMIZER

D. Ferrando,[1,*] M. Carreres,[2] M. Belmar-Gil,[2] D. Cervelló-Sanz,[2] B. Duret,[1] J. Reveillon,[1] F.J. Salvador,[2] & F.X. Demoulin[1]

[1]*CNRS CORIA UMR 6614, Université de Rouen Normandie, CNRS University and INSA of Rouen, Saint Etienne du Rouvray 76800, France*

[2]*CMT-Motores Térmicos, Universitat Politècnica de València, Camino de Vera s/n, Valencia, E-46022, Spain*

*Address all correspondence to: D. Ferrando, CNRS CORIA UMR 6614, Université de Rouen Normandie, CNRS University and INSA of Rouen, Saint Etienne du Rouvray 76800, France, E-mail: diego.ferrando@coria.fr

Original Manuscript Submitted: 02/dd/2022; Final Draft Received: mm/dd/yyyy

Numerical simulations of simplex pressure-swirl atomizers can aid their design process towards better atomization. This work aims at studying the two-phase flow at both the internal geometry and the first millimeters of the external domain of such atomizers, where primary breakup takes place. In particular, the atomizer under study has been used in the CORIA Rouen Spray Burner (CRSB) test rig, which aims at studying lean premixed turbulent combustion. Ultimately, our goal is to complete the spray characterization in the vicinity of the injector. Such data will potentially enforce the validity of numerical simulations of non-reacting and reacting flow for this burner. Injection characteristics are analyzed through an interface capturing method within a detailed numerical simulations framework. The importance of the internal flow simulation on the final result is demonstrated in the manuscript, but it requires to accurately measure the injector internal geometry. In the present investigation, an experimental methodology combining different techniques is applied to this end, obtaining and parameterizing the actual geometry of the internal ducts within the atomizer. The numerical workflow is divided in two simulations, to separately study the internal flow formation and the external spray development. This division is proposed given the difficulty to mesh the whole computational domain handling all the present length scales while still preserving the required accuracy. Several mesh refinements are studied for each simulation, also analyzing the coupling between the related internal and external simulations. The methodology is validated against experimental data for two CRSB operating conditions. The investigation then proves it is possible to couple the internal and external flow in order to describe the actual air core formation, liquid film behavior and breakup mechanism of these atomizers, extracting relevant atomization outputs in the near-field region where experimental data are scarce.

KEY WORDS: *internal flow; primary atomization; pressure-swirl atomizer; geometry measurement; pre-processing; Large-Eddy Simulation; Volume of Fluid*

1. INTRODUCTION

Simplex pressure-swirl atomizers have engineering applications in several fields, such as agricultural spraying, fire suppression, spray painting, spray cooling, spray drying for food or pharmaceutical processing and different combustion applications. Focusing on thermal engines, spray characteristics strongly influence their performance, fuel consumption and emissions generation (Lefebvre and Ballal, 2010). Even though the industry and transportation sectors are progressively being decarbonized, air transport will still need to rely on fossil fuels for some time due to the large power requirements (European Commission, 2020). In this regard, state of the art of aero engines (such as the lean-burn GE-TAPS) tend to use airblast atomizers together with simplex pressure-swirl atomizers, the latter generating the pilot flame for the startup and low-power regimes (Mongia, 2003).

In simplex pressure-swirl atomizers, fuel is fed to a spin chamber through several tangential ports before being injected through the atomizer outlet (Lefebvre and McDonell, 2017). This situation is depicted in Figure 1. If the Reynolds number (Re) is above a given threshold, the swirling motion generated in the spin chamber induces a depression that pulls external air inside the atomizer, shaping the so-called air core (Som, 2012). Hence, the fuel is forced to stick to the walls in the shape of a film, being injected into the environment as a hollow cone. (Chinn, 2009) reviewed some earlier works and developed an inviscid flow analysis to justify the discharge coefficient, air core radius and spray cone angle evolution observed for this kind of atomizer as a function of the so-called *atomizer constant*, which embeds the relevant atomizer dimensions. (Park et al., 2007) found the liquid temperature can influence the air core stability through Re, defining an unstable and a transitional regime. The initial liquid film thickness at the atomizer outlet can be derived from these estimations.

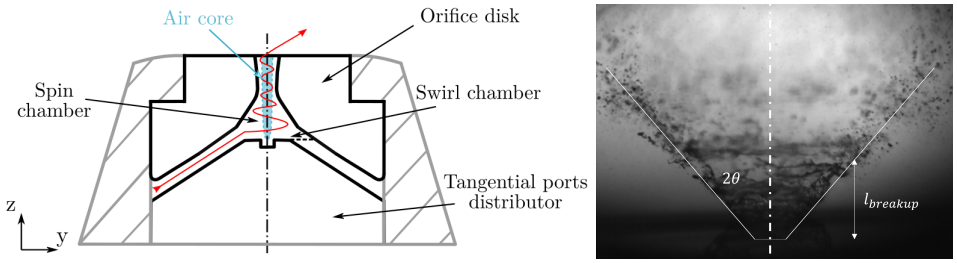

FIG. 1: Left: Cross-section sketch of the upper part of a simplex Danfoss pressure-swirl atomizer and paths for the liquid (red) and air (light blue). Right: Spray cone angle (2θ) and primary break-up length ($l_{breakup}$) represented over a shadowgraphy picture Verdier et al. (2017).

Leaving the internal flow aside and focusing on the atomizing features, simplex pressure-swirl atomizers have drawn the attention of both experimentalist and modelling researchers. From the experimental side, the techniques employed include Mie-scattering (Liu et al., 2019), Phase Doppler Anemometry (PDA) (Dafsari et al., 2019; Leask et al., 2019; Maly et al., 2019), Laser Doppler Anemometry (LDA) (Laurila et al., 2020), Particle Induced Velocimetry (PIV) (Durdina et al., 2014; Jedelsky et al., 2018) or high speed shadowgraphy Rajamanickam and Basu (2016). These investigations qualitatively show that primary breakup is produced by the growth of a Kelvin-Helmholtz instability on the liquid sheet as soon as the fuel leaves the atomizer and interacts with the surrounding gas. Numerical methods may enhance the study of

swirling sheets granting access to zones where experiments can barely access. In commercial injectors, the internal fuel flow can not be determined by experimental means. Even the near-nozzle region could be difficult to visualize by current optical techniques, requiring modifications on the injector geometry to obtain optical access. Numerical simulation can then bridge the gap among the near and the far-field by offering a level of detail that experiments can scarcely offer.

In this way, from the computational point of view, most investigations make use of diverse Volume of Fluid (VOF) methods that deal with the two-phase flow in a fully Eulerian framework. All turbulence modelling approaches have been used, including the laminar assumption (Amini, 2016; Razeghi and Ertunç, 2018), Reynolds-Averaged Navier-Stokes (RANS) (Alajbegovic et al., 2002) and Large-Eddy Simulation (LES) (Laurila et al., 2019). Even though these works cover both the internal and the external flow simultaneously, they do not seem to reproduce the liquid sheet instabilities that have been observed to produce breakup, and thus predict atomization mechanisms that might differ from the actual one. Except for (Laurila et al., 2019) (with an atomizer configuration fairly different from those used for combustion applications), only investigations using computationally expensive Direct Numerical Simulation (DNS) either through VOF (Fuster et al., 2009; Galbiati et al., 2016) or Level Set (Shao et al., 2017) do capture liquid film instabilities triggering atomization. (Shao et al., 2017) realized they needed to prescribe a turbulent inflow condition in order to reproduce these fluctuations, highlighting the role of turbulence on the process.

The objective of the present investigation is to present a methodology to numerically analyze primary atomization in simplex pressure-swirl atomizers. The atomizer mounted in the CORIA Rouen Spray Burner (CRSB) is particularly investigated, considering this configuration was studied as a reference for gas turbine applications in the last Turbulent Combustion of Sprays workshops (TCS: `http://www.tcs-workshop.org`). Hence, some spray features in the spray secondary breakup region (Shum-Kivan et al., 2017; Verdier et al., 2017) and combustion outcomes (Mulla et al., 2019a,b; Mulla and Renou, 2019) have already been determined experimentally. The present investigation thus aims at filling the gap between this far-field region and the atomizer outlet, where experimental data can scarcely be obtained, as stated. The proposed methodology includes three pre-processing stages, namely the experimental determination of the atomizer internal geometry, the mesh generation and the definition of a numerical setup able to handle this multi-scale problem. Eventually, a realistic simulation of the complete flow from inside the injector up to the end of the primary break-up allows us predicting the spray size distribution following the method proposed by (Palanti et al., 2022).

2. EXPERIMENTAL GEOMETRY CHARACTERIZATION

The first pre-processing step towards numerically modelling the internal flow and atomization process is to determine the computational domain. The pressure-swirl atomizer mounted in the CRSB is a commercial Danfoss OD-H 030H8103 oil nozzle. This is a hollow-cone atomizer manufactured in accordance with European standard EN 293 with a nominal opening angle of $80°$ and a nominal mass flow rate of $1.35\,\mathrm{kg/h}$.

As shown in Figure 1, two of the injector pieces (namely the tangential ports distributor and the orifice disk) shape the internal geometry of the atomizer. This includes three inlet fuel ports, the swirl and spin chambers and the orifice itself. The atomizer internal geometry has then been characterized through a combination of experimental techniques applied to the aforementioned pieces:

- Computed Tomography scan (CT-Scan).
- Optical microscope visualization.
- Scanning Electron Microscope (SEM) visualization.

Additionally, a caliper was used to measure the global dimensions of the atomizer pieces. The techniques, described in the following subsections, have been applied either to:

- The disassembled metallic pieces, or
- Silicon molds of the atomizer pieces, obtained as introduced by (Macian et al., 2003) for diesel injector nozzles.

This methodology has been described by (Salvador et al., 2018), who validated its use when determining the internal features of a Diesel injector. The reader is referred to this work for a detailed description of the techniques and a comparison of their advantages and limitations.

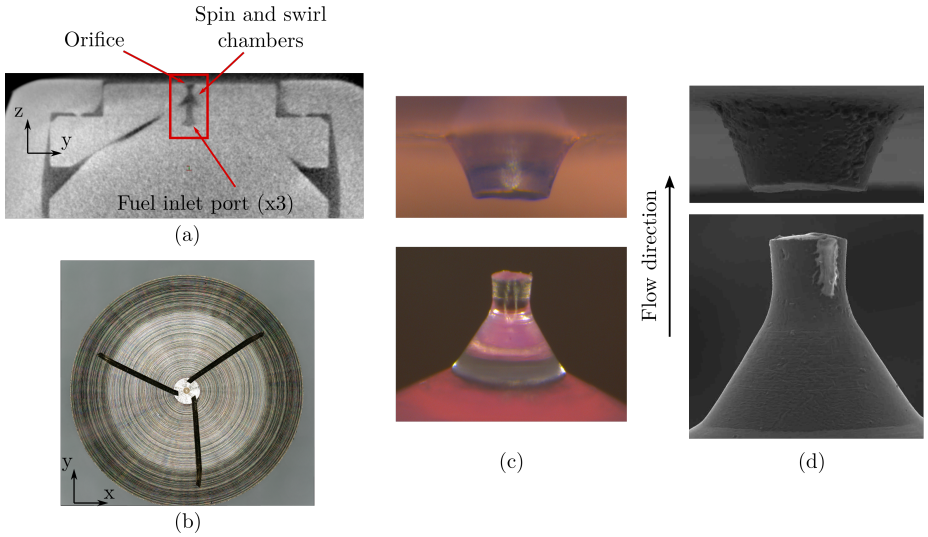

FIG. 2: Sample pictures of the internal geometry of the CRSB atomizer: (a) CT-Scan visualization of the upper part of the atomizer assembly; (b) Optical microscope visualization of the tangential ports distributor piece, top view; (c) Optical microscope visualization of the silicon molds of the spin and swirl chambers, side view; (d) SEM visualization of the silicon molds of the spin chamber, side view.

2.1 Computed Tomography scan (CT-Scan)

The Computed Tomography allows obtaining tomography cuts of the atomizer pieces in non-transversal planes. These images are then used to reconstruct the full 3D geometry. A Nikon XT H-160 CT-Scan machine able to produce x-ray beams with a power up to 60 W at a maximum voltage of 60 kV was used.

The resolution achieved by this technique depends on the particular geometry and the material that the beams have to travel through. The produced images in this application have a maximum magnification of 150x and a pixel size in the order of 10 µm. This resolution is poorer

than the one reached with the other techniques, but it is the only one that allows visualizing the full atomizer assembly, as shown in Figure 2(a). Hence, in this investigation it has only been used to validate the other two techniques and to help determining the orifice contour.

2.2 Optical microscope visualization

A Leica MZ APO system with up to 80x magnification has been used. It mounts a PLANAPO 1.0X objective and a KL1500 optic fiber illuminator.

Figure 2(b) and Figure 2(c) show samples of visualization corresponding to a disassembled metallic piece and the silicon molds of the CRSB atomizer, respectively.

2.3 Scanning Electron Microscope (SEM) visualization

A Jeol JSM6300 Scanning Electron Microscope (SEM) has been employed. It operates at $30\,\mathrm{kV}$ and offers a magnification up to 1000x.

The SEM requires the observed sample to be conductor. Hence, the silicon molds need to be covered by a thin layer (in the order of nm) of gold dust. The accuracy of the technique was reported to be around 2% (2-3 $\mu\mathrm{m}$) in the determination of injector nozzle orifices outlet diameter Salvador et al. (2018).

Figure 2(d) shows an example of SEM visualization of the CRSB atomizer silicon molds of the spin chamber.

2.4 Geometry parameterization

From visualization through the aforementioned techniques it is possible to parameterize the atomizer geometry, as shown in Figure 3. This parameterization allows generating CAD volumes for CFD modelling purposes and enables sensitivity studies on the geometry through the variation of the parameter values.

Collecting images through optical microscope and SEM visualization allowed determining the values of the geometrical parameters of the actual CRSB atomizer unit. A given parameter can be obtained through several images with different techniques or different magnification rates. A mean value and standard deviation can then be determined for each parameter.

Results from the application of the techniques are summarized in Table 1 together with the values finally accepted to build the computational domain. It must be noted that the parameterization depicted in Fig. 3 over-restricts the geometry. Hence, the values accepted for the computational domain need to re-balance all parameters so they are compatible with each other. This was done by prioritizing the parameters whose determination is deemed to be more reliable (for instance, linear distances are prioritized to rounding radius or angle measurements).

3. NUMERICAL STRATEGY

Due to the large range of length scales to be considered, about several millimeters for injector scale down to few microns for the liquid film and drop size, the present work proposes a two steps coupling methodology: first, the internal flow of the injector is modelled; afterwards, an external simulation is set up to predict the early stage of the atomization process. Both numerical simulations are carried out using the same numerical methods to preserve consistency among them.

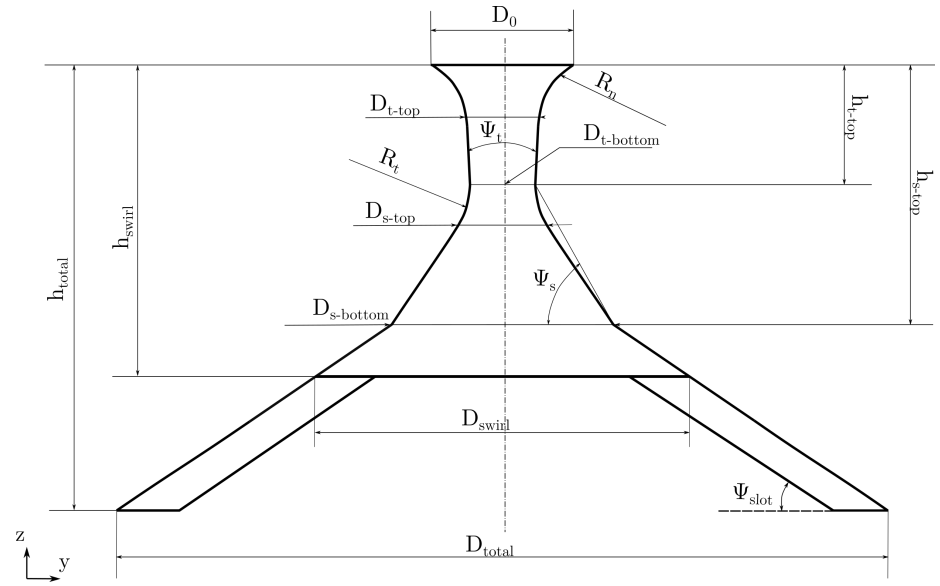

FIG. 3: Abstraction of the Danfoss OD-H nozzle with the defined geometrical parameterization (over-constrained).

3.1 Numerical methods

The numerical simulation is based on the well known *OpenFoam 6.0* library, which already contains many features needed for liquid-gas flows simulation involving complex geometries (The OpenFoam Foundation, 2018). The chosen solver is the *interFoam* multiphase solver. This solver is based on the Volume of Fluid (VoF) method, introducing the liquid volume fraction ($\alpha = \frac{V_l}{V_{cell}}$) as a relevant magnitude in each cell. The Interface Capturing Method (ICM) is based on a sharpening term that aims at preserving a sharp transition through the liquid-gas interface (i.e. where the liquid volume fraction takes values different than 0 or 1). The description is based on mass and momentum equations:

$$\frac{\partial \bar{u}_j}{\partial x_j} = 0 \tag{1}$$

$$\frac{\partial \bar{\rho}\bar{u}_i}{\partial t} + \frac{\partial}{\partial x_i}(\bar{\rho}\bar{u}_j\bar{u}_i) = -\frac{\partial \bar{P}}{\partial x_i} + \frac{\partial}{\partial x_j}\left(\tau_{ij} + \tau_{tij}\right) + \bar{\rho}g_i + f_{\sigma i} \tag{2}$$

where $\bar{u}$ represents the velocity vector, $\bar{P}$ the pressure, $\bar{\rho}$ the density of the cell mixture (defined as $\bar{\rho} = \bar{\alpha}\rho_l + (1-\bar{\alpha})\rho_g$, τ_{ij} and τ_{tij} the viscous and turbulent stresses including all sub-grid scale effects. Regarding turbulence, since it is not possible to solve all scales present in the flow, an unresolved flow at sub-grid scale has to be considered. The LES approach for single-phase flows is widely spread and applied with success, but it should be adapted to handle sub-grid liquid-gas flow interaction. However, direct application of the LES formalism to multiphase flows brings a lot of difficulties yet to be solved (see for instance Chesnel et al. (2011)). Accordingly, most published studies undertake the strategy of using an interface capturing method to track the liquid-gas interface together with single-phase flow LES models for the dynamics. The present work undertakes this approach, which requires to specify the LES model used to

Parameter	Unit	Dimensions				
		Optical micr. (molds)	SEM (molds)	SEM (direct visualization)	CT	Accepted
D_0	µm	313 ± 2	300 ± 2	298 ± 1	301 ± 3	300
D_{t-top}	µm	179 ± 4	180 ± 5	-	-	180
$D_{t-bottom}$	µm	164 ± 2	160 ± 1	160 ± 1	169 ± 3	165
D_{s-top}	µm	209 ± 3	213 ± 2	-	-	210
$D_{s-bottom}$	µm	491 ± 5	480 ± 5	496 ± 2	500 ± 1	500
D_{swirl}	µm	774 ± 6	781 ± 6	776 ± 2	773 ± 4	780
D_{total}	µm	-	-	3492 ± 1	3375 ± 1	3375
h_{t-top}	µm	233 ± 4	238 ± 3	-	-	240
h_{s-top}	µm	532 ± 6	546 ± 3	-	540 ± 2	540
h_{swirl}	µm	600 ± 5	605 ± 4	-	600 ± 2	620
h_{total}	µm	-	-	-	2400 ± 1	2400
R_n	µm	303 ± 5	300 ± 4	-	-	308
R_t	µm	171 ± 6	191 ± 5	-	-	190
ψ_t	°	6 ± 4	6 ± 2	-	-	6
ψ_s	°	57 ± 6	58 ± 4	-	-	61
ψ_{slot}	°	27 ± 6	28 ± 3	-	-	30

TABLE 1: Summary of the results obtained from each metrology technique and *accepted* values to construct the inner computational domain.

prescribe the sub-grid stress. In previous works Anez et al. (2019), comparisons between several models showed the ability of the WALE model Nicoud and Ducros (1999) to capture flow instabilities in wall boundary layers for liquid gas flow with low mesh resolution. Hence, this is the model chosen for the present study.

Additionally, g_i the gravitational acceleration, whereas f_σ represents the surface tension forces, calculated as:

$$f_\sigma = \sigma\kappa\frac{\partial\bar{\alpha}}{\partial x_j} \tag{3}$$

where σ is the surface tension between the liquid and the gas, α is the liquid volume fraction and κ is the curvature of the liquid, computed as:

$$\kappa = -\frac{\partial}{\partial x_j}\left(\frac{\partial\bar{\alpha}/\partial x_j}{|\partial\bar{\alpha}/\partial x_j|}\right) \tag{4}$$

In order to determine the interface position, an equation for the liquid volume fraction α advection is solved:

$$\frac{\partial\bar{\alpha}}{\partial t} + \frac{\partial(\bar{\alpha}\bar{u}_j)}{\partial x_j} + \frac{\partial(U_j^r\bar{\alpha}(1-\bar{\alpha}))}{\partial x_j} = 0 \tag{5}$$

The interface is implicitly captured through Eq. 5. Thus, as stated, the interface is localized at the transition between the gas ($\alpha = 0$) and the liquid ($\alpha = 1$). In order to keep an accurate

description of the interface, the transition should remain sharp with a size in the order of few Δx. Regular VOF approaches reconstruct the interface position (Scardovelli and Zaleski, 1999), considering the liquid volume flux based on the geometrical advection of this surface. This geometrical approach is unsuitable if the polyhedra generally used in OpenFoam to handle complex geometry are chosen as numerical cells, since liquid advection is based on standard numerical schemes bringing numerical diffusion that potentially enlarge the liquid-gas transition zone. A sharpening term is introduced to counter this effect and compress the interface region thanks to the use of an artificial velocity field, U_j^r, defined as a relative velocity between the two phases (Rusche, 2002; Wardle and Weller, 2013).

As far as the numerical schemes are concerned, the *backward Euler* second order scheme and the hybrid first-second order *CrankNicolson* scheme Crank and Nicolson (1947) are used for the time derivatives. The *CrankNicolson* scheme requires a blending factor, which is chosen as 0.9 in order to remain close to second order while preserving stability. The convection schemes are either *limitedLinear* (linear scheme stabilized with the introduction of a Sweby limiter Sweby (1984)) or *van Leer* van Leer. (1974), both tending to second order accuracy. Finally, a MULES procedure (Boris and Book, 1968) has been used to enforce liquid mass conservation by avoiding undershooting and overshooting the liquid volume fraction at each cell.

3.2 Operating conditions

The operating conditions studied in this work replicate the ones experimentally studied by (Verdier et al., 2017), corresponding to atmospheric pressure and temperature (i.e. no fuel preheating). Given that *interFoam* is an incompressible isothermal solver, the density ρ and the kinematic viscosity ν for both the fuel (n-heptane) and air remain constant. Also, the surface tension σ between the two fluids is needed. The values of the parameters used in the simulation at the studied temperature are reported in Table 2.

	$T[K]$	$\rho[kg/m^3]$	$\nu[m^2/s]$	$\sigma[mN/m^2]$
Fuel	298	678.9	$5.67e-07$	20.0
Air	298	1.117	$1.57e-05$	

TABLE 2: Fuel and air properties used in the simulations.

4. INTERNAL FLOW MODELLING

4.1 Numerical domain, mesh and boundary conditions

The choice of the computational mesh topology is an important step in a multiphase flow simulation. The maximum resolution needs to be enough to capture the interface between the liquid and the gas, but it should still keep a manageable simulation of the whole geometry. Literature studies on pressure-swirl atomizers (Hansen et al., 2002; Sumer et al., 2012) used full hexahedral structured meshes because they allow modifying the cell size of the regions of interest in a straightforward manner. Nevertheless, the inlet ports of the injector of study are placed with a certain tilting angle with respect to the swirl chamber, preventing the geometry from being fully meshed trough structured hexahedral elements. Several configurations have been tested exclusively keeping hexahedral elements, since according to the authors experience they provide

a more accurate resolution of the liquid-gas flow within *interFoam*. Nevertheless, the tested approaches induced a high number of hexahedral cells with high values of the skewness, aspect ratio and non-orthogonality, producing poor quality meshes that eventually reduced the global accuracy of the methodology. Several attempts were performed to improve the mesh quality keeping a fully structured approach, but none of them was successful.

In order to overcome the aforementioned problem, the approach used by (Madsen et al., 2004) or (Ding et al., 2016) was adopted, utilizing a strategy based on a hybrid tetrahedral-hexahedral mesh. The main idea of this approach is to keep as much hexahedral elements as possible everywhere in the domain, except for the conflicting zone. Accordingly, a ring of tetrahedral elements is placed in the region where the tangential ports intersect the swirl chamber. The rest of the domain (i.e. the three tangential ports, the body of the injector and also the external zone of the domain) is composed by hexahedral elements following a structured mesh.

A representation of the final mesh strategy is shown in Figure 4, where the different cell topologies are represented.

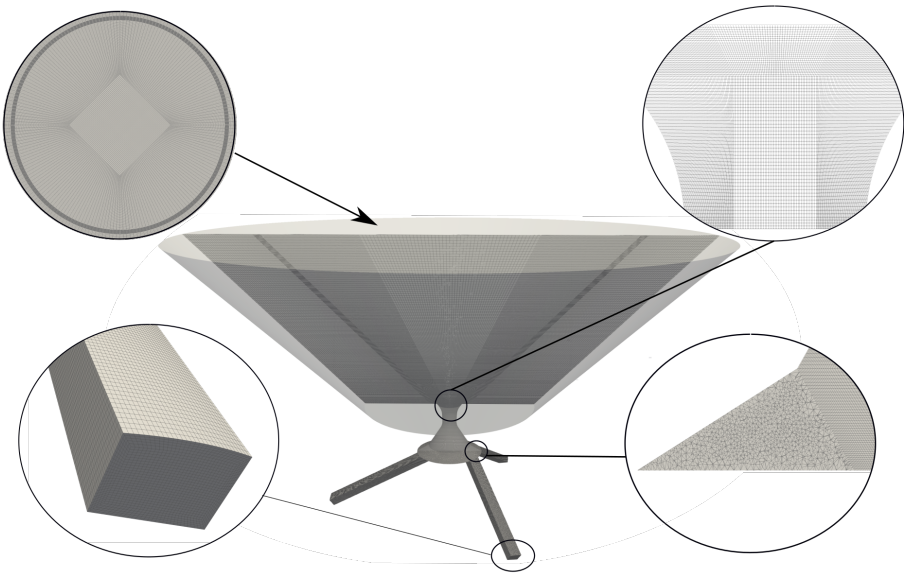

FIG. 4: Computational grid sketch. Hybrid mesh made of hexahedral and tetrahedral elements.

Three boundary zones are defined to set up the boundary conditions: the tangential ports inlet, the inner injector walls and the outlet boundary surface corresponding to the atmosphere. Those zones are represented in Figure 5: green for the inlet patches (number 1), grey for the wall patches (number 2) and blue for the outlet patches (number 3).

At the inlet, the fuel mass flow rate $\dot{m}_{fuel} = 0.28 g/s$ (corresponding to the CRSB operating condition) is equally divided among the three tangential ports. This imposes the boundary condition for the velocity as a fixed mass flow rate in each tangential port. The pressure gradient is fixed as $\nabla p = 0$ and a fixed value is used for the liquid volume fraction, with $\alpha = 1$ (i.e. only liquid entering the domain through the inlet).

The walls are set up with usual boundary conditions. Therefore, a no-slip boundary condition is set for the velocity, whereas Neumann boundary conditions are used for the pressure ($\nabla p = 0$) and liquid volume fraction ($\nabla \alpha = 0$).

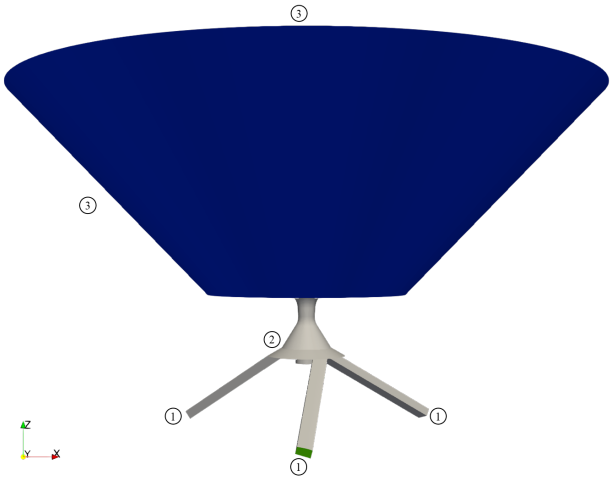

FIG. 5: Boundary conditions patches of the CRSB internal flow simulation.

Finally, in the case of the *outlet* patch, Neumann boundary conditions are imposed for the velocity ($\nabla \mathbf{u} = 0$) and for the liquid volume fraction ($\nabla \alpha = 0$). The *totalPressure* boundary condition is used and fixed to atmospheric pressure. This boundary condition sets the value of the patch pressure as follows:

$$p_p = p_0 - \frac{1}{2}|\mathbf{u}|^2 \tag{6}$$

where p_p is the patch pressure, p_0 is the total pressure given to the boundary, and the last term $\frac{1}{2}|\mathbf{u}|^2$ represents the dynamic pressure.

A summary of the boundary conditions is reported in Table 3:

	1. Inlet	**2. Wall**	**3. Outlet**
$\mathbf{u}$	**D**: imposed flux	**D**: $\mathbf{u} = 0$	**N**: $\nabla \mathbf{u} = 0$
p	**N**: $\nabla p = 0$	**N**: $\nabla p = 0$	**D**: totalPressure
α	**D**: $\alpha = 1$	**N**: $\nabla \alpha = 0$	**N**: $\nabla \alpha = 0$

TABLE 3: Boundary conditions used at the different domain patches. **D**: Dirichlet boundary condition. **N**: Neumann boundary condition.

The computation has been run with several mesh resolutions in order to carry out a mesh convergence study. The main features of the computational grids are shown in Table 4. At least 85% of the cells are hexahedral cells in all cases. The main goal when refining from the coarsest to the finest mesh was to increase the number hexahedral elements trying to keep the number of tetrahedral elements as low as possible. At the bottom of the table, the maximum and averaged values for y^+ are shown at different zones of the geometry.

In order to reduce the global amount of computational resources spent, the simulations are not run from the beginning for all three meshes. The initialization is performed with the coarse mesh only, until the flow reaches a steady regime. Afterwards, the computed fields are mapped into the subsequent more refined meshes to resume the calculations. This methodology produces a new pseudo-transient at each mapping step, but reduces the global computational resources

	Coarse Mesh		Medium Mesh		Fine Mesh	
Number of elements	2.7e6		13.2e6		32.8e6	
Tetrahedra	0.13e6		1.6e6		3.2e6	
Hexahedra	2.6e6		11.6e6		29.6e6	
Pyramids	4.3e3		11.7e3		24.9e3	
Y^+	Max	Avg	Max	Avg	Max	Avg
Full geometry	66.1	12.1	21.8	2.6	3.4	1e-2
Inlet ports	66.1	9.2	21.8	2.8	1.7	0.78
Swirl Chamber	28.5	12.8	11.3	3.7	3.4	0.96
Spin Chamber	13.7	3.2	2.9	1.3	2.7	1.8
Throat	24.6	13.8	3.3	2.4	2.3	1.8
Nozzle	33.4	21.5	3.5	2.6	2.8	2.2

TABLE 4: Features of the meshes used for the internal flow simulations.

	Coarse Mesh	Medium Mesh	Fine Mesh
Δt	5e-9 s	2.5e-9 s	5e-10
$CPUs$	112	420	672
Δt_{real}	0.26 s	0.6 s	2.9 s
$CPUh/ms$	1.6e3	28e3	1e6

TABLE 5: Computational resources used for the internal flow computations.

used to compute the transient stages of the injection for all meshes. The CPU-hours finally used with each mesh are collected in Table 5.

4.2 Initialization: Time evolution of hollow cone generation

It may be important for some regimes to have a clear understanding of the liquid flow establishment once the fuel emanates from the orifice section. Considering the boundary and initial conditions, a certain amount of time is required by the fluid to establish the cone-shaped flow (Razeghi and Ertunç, 2018).

Figure 6 shows the time evolution of the air core generation and the hollow cone shape of the spray. Figure 6(a) represents the initial conditions of the simulation, where the fuel fills the whole injector. From Figure 6(b) to Figure 6(d), the fuel is expelled in a distorted pencil shape. Later on, starting from Figure 6(f), the jet begins to break-up. In Figure 6(i) it starts exhibiting a conical shape, still closing back at some distance downstream of the orifice. From Figure 6(k) the hollow cone spray opens and becomes established, meaning the cone angle and the liquid film thickness can be measured. Nevertheless, the air core is not fully developed yet, making it necessary to compute additional 250μs for this to happen. Once the air core finishes developing, it reaches the bottom wall of the injector and it widens. To summarize, the total time to initialize the simulation (i.e. the transient period of the injector from rest to nominal conditions) was in the order of $0.5ms$.

4.3 Liquid volume fraction

As stated in Section 4.1, the initialized results from the coarser mesh (velocity, liquid volume fraction and pressure fields) are mapped into the medium and fine resolution meshes. Figure 7

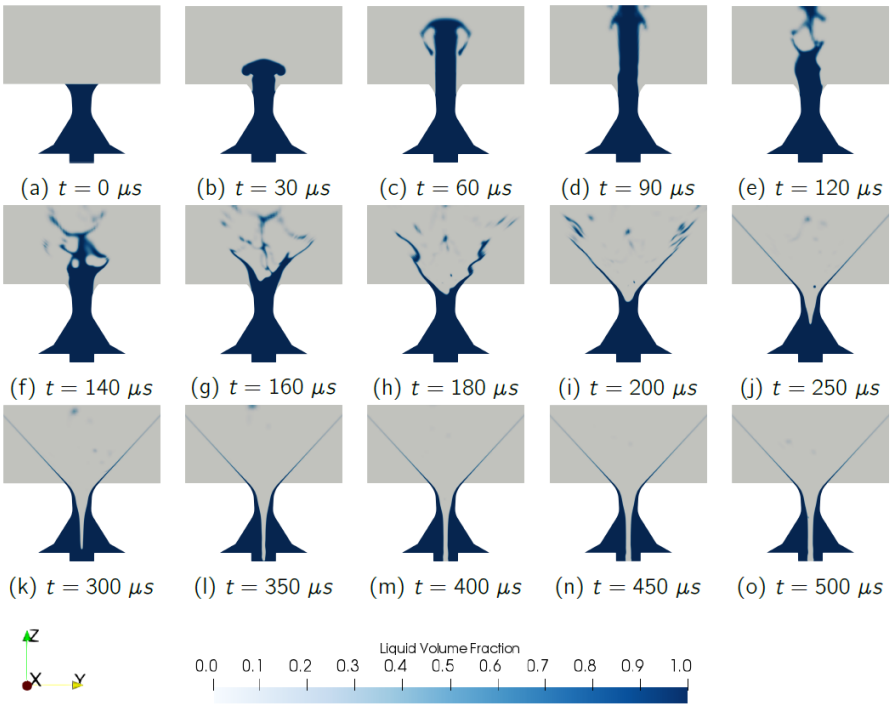

FIG. 6: Hollow cone transient evolution depicted through liquid volume fraction contours at the domain mid-plane.

shows a mid-plane contour of the liquid volume fraction α for each mesh resolution, once the pseudo-transient after mapping to each mesh is finalized. It can be observed that the coarser mesh is not able to capture as much instabilities at the bottom zone of the air core as the other two meshes. Simulations with the most refined meshes do show instabilities at the air core. This phenomenon has already been reported in other studies about simplex swirling injectors, such as (Sumer et al., 2012) or (Maly et al., 2018). Regarding these instabilities, no remarkable differences are seen between the medium and fine meshes.

Figure 8 shows iso-contours of liquid volume fraction ($\alpha = 0.5$) representing the liquid-gas interface for each of the three meshes. It is observed that the air core thickens for the medium and fine meshes, but no substantial differences are found between cases at the external part of the domain.

Figure 9 shows experimental pictures reported by (Verdier et al., 2017) for illustrating purposes. The comparison between Figure 8 and Figure 9 indicates a poor agreement of the numerical computation with the experimental images, due to a lack of resolution at the external zone, downstream of the nozzle orifice outlet. For the nearly structured mesh approach adopted for this simulation, increasing the cell resolution at the external part would also imply having more additional cells for the internal part of the domain, where Figure 7 and Figure 8 proved they are not necessary. This fact drove the authors to divide the problem in two parts, so that the external spray could be analyzed by means of a dedicated simulation with a different mesh strategy, as presented in Section 5.

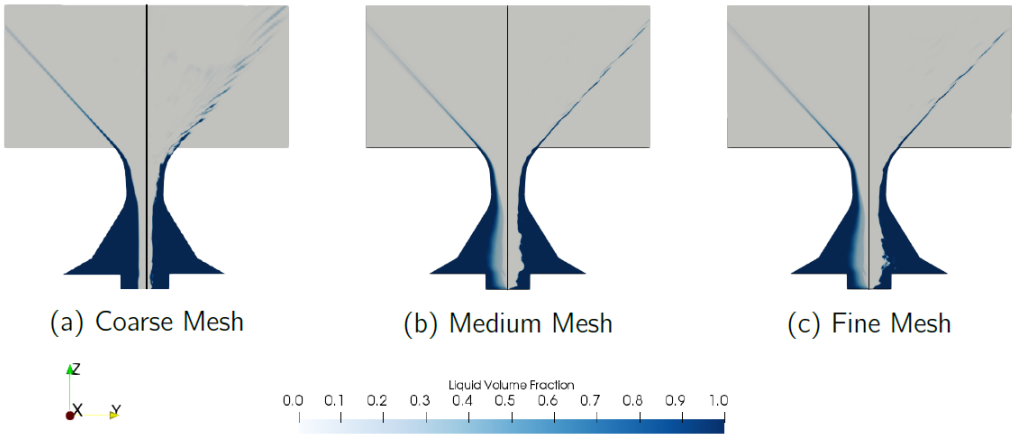

FIG. 7: Liquid volume fraction contours at the domain mid-plane for the three mesh resolutions presented. In each case, the left-hand side represents time-averaged data, whereas the right-hand side depicts instantaneous data.

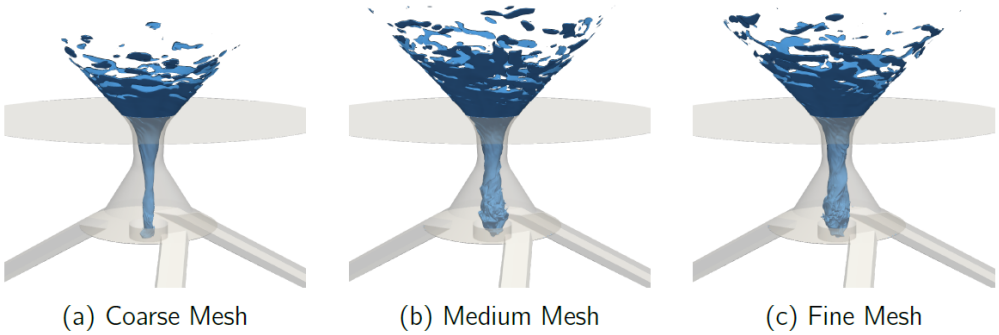

FIG. 8: Liquid volume fraction iso-contour for $\alpha = 0.5$.

4.4 Liquid film thickness

The liquid film thickness is retrieved at the nozzle orifice for the three cases. The film thickness remains almost constant in time in the coarse mesh case. However, as the numerical grid is refined, the liquid film begins to fluctuate. In order to allow for comparison among cases, Figure 10 shows the time averaged liquid volume fraction ($\bar{\alpha}$) radial profile at the nozzle orifice. The thickness of the liquid film is $t_l^{coarse} = 24 \pm 4\mu m$ for the coarse case, whereas both the medium and fine meshes yield a value of $t_l^{fine} = 22 \pm 15\mu m$. These numerical values are compared against empirical equations in order to assure the effectiveness of the method. An evaluation of the most known semi-empirical correlations for pressure-swirl atomizers is carried out in Nural and Özgür Ertunç (2018) and used as a reference for this study. Additionally, another method to calculate the film thickness is proposed. The theoretical liquid film thickness is computed in this case through a discharge coefficient (C_D) empirical correlation, as follows. First, C_D is

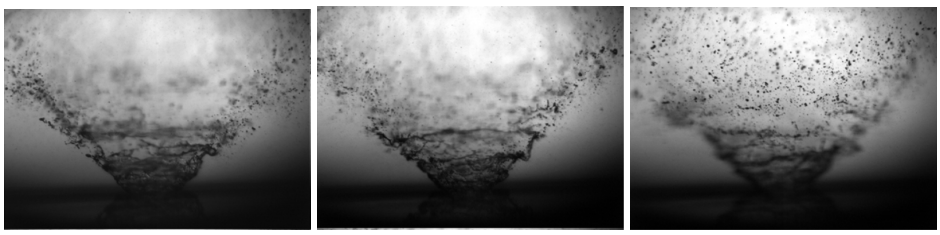

FIG. 9: Sample experimental pictures by (Verdier et al., 2017) for three different instants.

calculated with its theoretical definition Lefebvre and Ballal (2010):

$$C_d = \frac{\dot{m}_{fuel}}{\dot{m}_{th}} = \frac{\dot{m}_{fuel}}{A_o\sqrt{2\Delta P\,\rho_{fuel}}} \tag{7}$$

Then, the ratio between the air core area (A_a) and the orifice area (A_o) is expressed as a function of the film thickness as:

$$X = \frac{A_a}{A_o} = \frac{\pi(d_o - 2t_l)^2/4}{\pi d_o^2/4} \tag{8}$$

from where:

$$t_l = \frac{d_o(1-\sqrt{X})}{2} \tag{9}$$

Equation 10, proposed by (Giffen and Muraszew, 1953) relates the discharge coefficient to the ratio between the air core and orifice areas:

$$C_d = 1.17\left[\frac{(1-X)^3}{1+X}\right]^{0.5} \tag{10}$$

In order to compute the liquid film thickness through this method, the discharge coefficient is first calculated through 7, with the fuel mass flow rate and the operating pressure obtained from experiments (Verdier et al. (2017)). Then, X is calculated iteratively from Equation 10. Finally, the film thickness is calculated through Equation 9

Figure 10 shows the values retrieved from the semi-empirical correlations compiled in Nural and Özgür Ertunç (2018) using the experimental pressure difference as operating pressure. The comparison between these equations and the simulation results is not straightforward, since the fluctuations within the atomizer yield a relatively wide range of film thickness values. In any case, the values obtained from the simulations are compatible with the correlation from Kim et al. (2010) and with the proposed method derived from the discharge coefficient. Both values are within the range. Older correlations provide values a varied range of values for the liquid film thickness. Simmons and Harding (1981) gives a small thickness value, close to the minimum recovered from the simulations. On the other hand, the thickness calculated according to Lefebvre and Suyari (1986); Rizk and Lefebvre (1985) is relatively close to the maximum thickness values obtained from simulations.

4.5 Spray cone angle

The spray cone angle is another characteristic parameter for simplex swirl atomizers. From the numerical study, it can be determined from Figure 7. The value of this angle (defined as 2θ

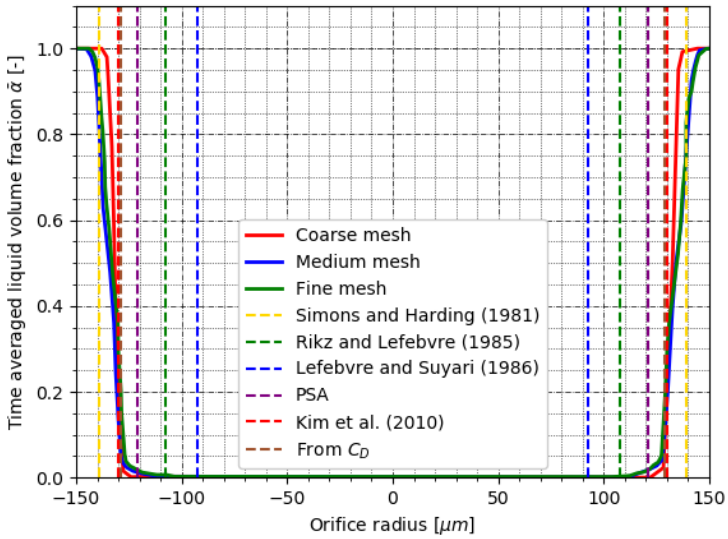

FIG. 10: Time averaged liquid volume fraction $\bar{\alpha}$ plot along the radial axis at the nozzle outlet. Red: coarse mesh; blue: medium mesh; green: fine mesh; dashed lines: empirical equations.

in Figure 1) is equal to 82°, matching the value of 80° (Verdier et al., 2017) obtained from experiments.

4.6 First-second order discretization effects

The mapping procedure described in Section 4.1 in order to transition from the coarsest mesh towards each subsequent finer mesh may create disturbances in the solution. In order to avoid numerical instabilities during this process, first order spatial schemes were used for this initial pseudo-transient found for each mesh. After running on the finer mesh for some time, these disturbances are damped and first order schemes could be fully replaced by second order schemes.

Figure 11 shows a comparison concerning the liquid film thickness appearance at the atomizer outlet cross-section for these two numerical schemes. It can be observed how first order schemes are more dissipative, not being able to capture instabilities in the liquid fuel sheet. Second order schemes, however, allow capturing those instabilities that could be responsible for triggering atomization.

In order to further investigate the role of these instabilities on primary breakup, results from both approaches (i.e. first order schemes leading to a smooth liquid sheet, and second order schemes capturing initial instabilities in the liquid sheet) were stored so they could be later mapped to the inlet of the dedicated external flow simulation. Results using mapped data for both approaches will be discussed in Section 5.

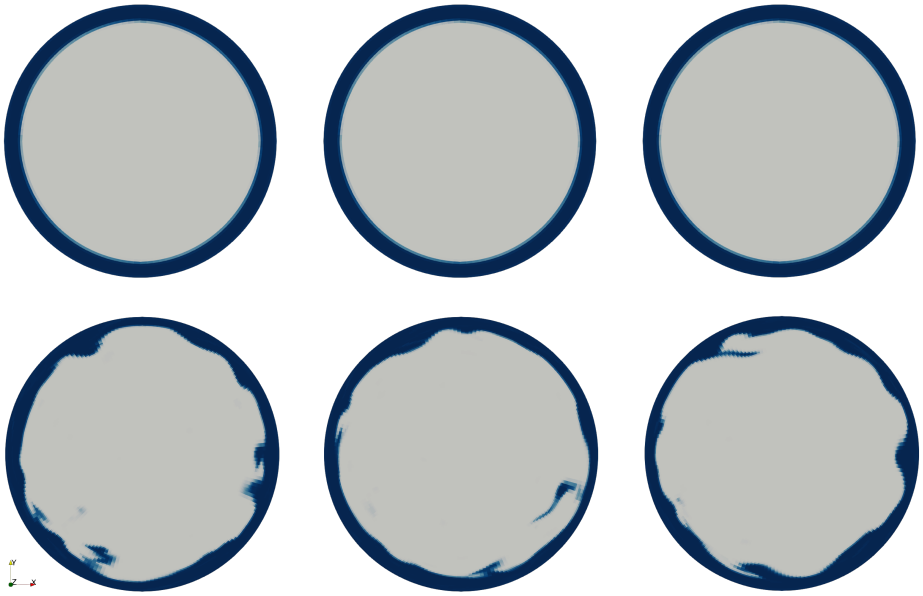

FIG. 11: Liquid volume fraction α contour at the atomizer outlet cross-section. Top: three snapshots using the *upwind* (first order) scheme for the spatial divergence. Bottom: three snapshots using the *limitedLinear* (second order) scheme for the spatial divergence. The time step between pictures is $\Delta t = 5\mu s$

5. EXTERNAL FLOW MODELLING: ZOOM ON THE ATOMIZATION PROCESS

In order to overcome the mesh resolution problem detected at the external zone of the fully integrated mesh shown in Section 4, a dedicated high resolution simulation is performed considering the outer part of the domain only. Focusing specifically on this part of the problem should allow reliably modelling the primary breakup mechanism of the pressure-swirl atomizer.

5.1 Numerical domain, mesh and boundary conditions

Figure 12 shows a sketch of the numerical domain and the boundary conditions considered for the external flow simulation. The angle of the sector is $\varphi = 45°$. The domain radius and height are 13 times the orifice diameter d_o ($r_{dom} = h_{dom} \approx 4mm$). These dimensions were defined following the work by (Galbiati et al., 2016).

Boundary number 1 is the inlet patch of the domain. It covers a surface starting from the orifice center up to an arc whose radius is equal to the injector orifice radius. The boundary conditions for the velocity **u** and the liquid volume fraction α are dynamically provided (i.e. time-varying) with the results from the previous internal flow simulation presented in Section 4. A Neumann boundary condition for the pressure is used in this case ($\nabla p = 0$). Boundary number 2, in turn, is treated as a wall boundary condition: a no-slip velocity boundary condition is set, specifying gradients at the wall equal to zero both for the pressure ($\nabla p = 0$) and the liquid volume fraction ($\nabla \alpha = 0$). Boundary number 3 is comprised by two periodic patches. Finally, boundary number 4 corresponds to the outlet of this simulation. As it was done in the previous simulation, the gradient of velocity (**u**) and the gradient of liquid volume fraction (α) are fixed to zero whereas the pressure p is set as a *totalPressure* condition, as already explained

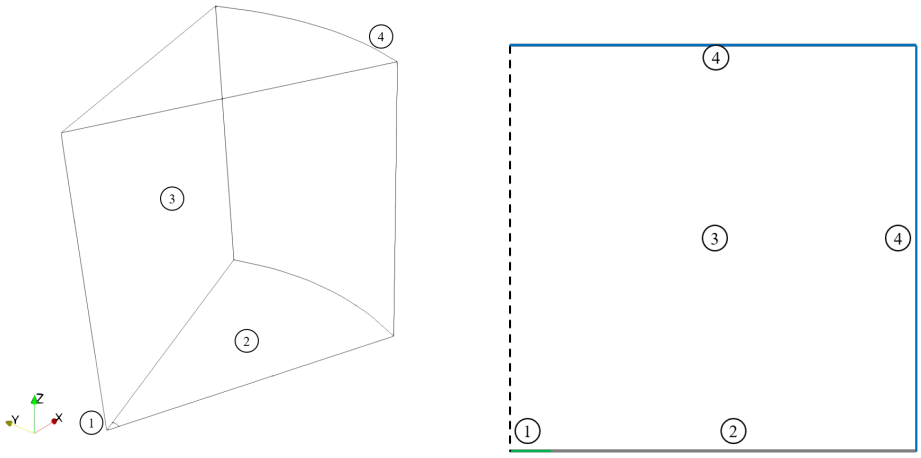

FIG. 12: Geometry domain and boundary conditions of the external flow simulation. Left: 3D view; right: view normal to a periodic patch. 1: Inlet; 2: Wall; 3: Periodic patches; 4: Outlet.

in Equation 6.

A summary of the boundary conditions is reported in Table 6:

	1. Inlet	**2. Wall**	**3. Periodic**	**4. Outlet**
u	**D**: time varying fixed value	**D**: $\mathbf{u} = 0$	periodic	**N**: $\nabla \mathbf{u} = 0$
p	**N**: $\nabla p = 0$	**N**: $\nabla p = 0$	periodic	**D**: totalPressure
α	**D**: time varying fixed value	**N**: $\nabla \alpha = 0$	periodic	**N**:$\nabla \alpha = 0$

TABLE 6: Boundary conditions for the external flow simulation. **D**: Dirichlet. **N**: Neumann

.

As far as the mesh strategy is concerned, an approach based on blocks of fully hexahedral structured elements is appealing to model the external breakup process. However, it was found to lead to additional issues. Due to the nature of such O-grids, the aspect ratio of the cells increases as a function of the radial coordinate. In this particular case, the liquid sheet follows a hollow cone shape, where the radial coordinates of the cells containing the sheet directly increase as the sheet is axially injected. This results in the mesh quality gradually worsening as a function of the axial coordinate. Hence, maintaining such a mesh strategy would not allow properly capturing the liquid sheet and the droplet formation process through an interface capturing method.

Numerical studies such as those performed by (Galbiati et al., 2016) or (Laurila et al., 2020, 2019) propose Cartesian isotropic meshes to model the breakup process of swirling injectors. Due to the aforementioned issues, the same approach is adopted in the present work.

In order to find the proper mesh resolution before running the actual 3D simulation, a small study with a 2D domain was performed for test purposes. In this study, a 2D structured Cartesian mesh is used assuming the problem to be axisymmetric. Table 7 reports the mesh information for three different meshes used in the 2D grid convergence study. Since these simulations are 2D, the number of cells increase by a factor of two every time the resolution is doubled. Given that the Courant number remains the same for the three cases, the time step Δt is also divided by two for each refinement level. Thus, the real time needed per iteration (Δt_{real}) also increases

by a factor of two.

	$2\mu m$	$1\mu m$	$0.5\mu m$
Number of elements	0.27e6	1.1e6	4.4e6
Cells at the liquid sheet	4	8	16
Δt	1.7e-8 s	0.8e-8 s	0.4e-8s
$CPUs$	72	72	72
Δt_{real}	0.92 s	1.8 s	3.7 s
$CPUh/ms$	$\approx$ 1000	$\approx$ 4500	$\approx$ 18500

TABLE 7: Information about the meshes used for the 2D grid convergence study of the external flow simulation.

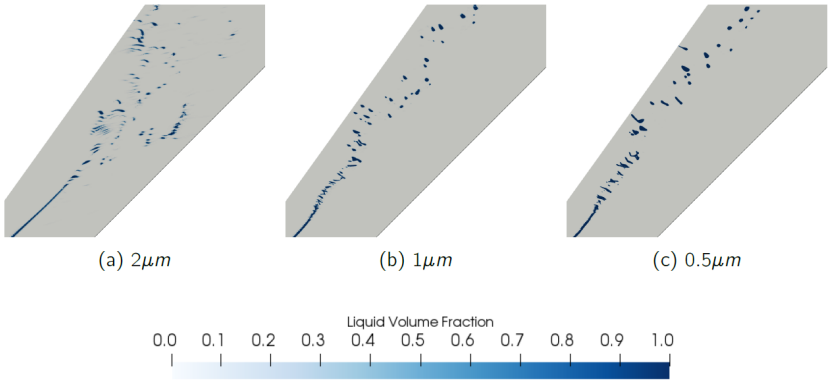

FIG. 13: Liquid volume fraction contours for different cell size cases in the 2D mesh convergence study for the external simulation. From left to right: $2\mu m$, $1\mu m$, $0.5\mu m$

Using the second order results from previous simulations as inputs at the inlet, Figure 13 shows the contour of liquid volume fraction α for the three different mesh cell sizes. All mesh resolutions tested are able to capture the interface between the liquid and the gas, not only for the liquid sheet but also for the 2D *droplets* produced during the breakup process. The main difference observed when comparing results for the different resolutions concerns the instability that develops along the liquid sheet, which is initial cause of breakup. Even though the mesh resolution in the $2\mu m$ cell size case is greater than the one showed in Section 4 for the external zone, this resolution is not enough to capture the liquid sheet instability triggered by the shear stress between the liquid sheet and the surrounding air. However, the cell size of $1\mu m$ allows capturing those fluctuations. Moreover, as expected, it provides a better interface capturing of the liquid sheet and the predicted shape of the 2D *droplets* is more realistic. Finally, the finest resolution also enforces the interface capturing effect but it does not significantly modify the appearance of the instabilities. For this reason, a cell size of $1\mu m$ is chosen as a reference for the 3D study.

Once the cell size is chosen from the 2D study, a 3D sector Cartesian mesh is set. Figure 14 shows a mid-plane cut of the mesh. The refinement zone defined to follow the spray cone angle can be observed, reaching up to 1.3 mm along the axial coordinate. The mesh has around 88 million elements, most of them with a characteristic size of $\Delta x = 1\mu m$. In order to complete

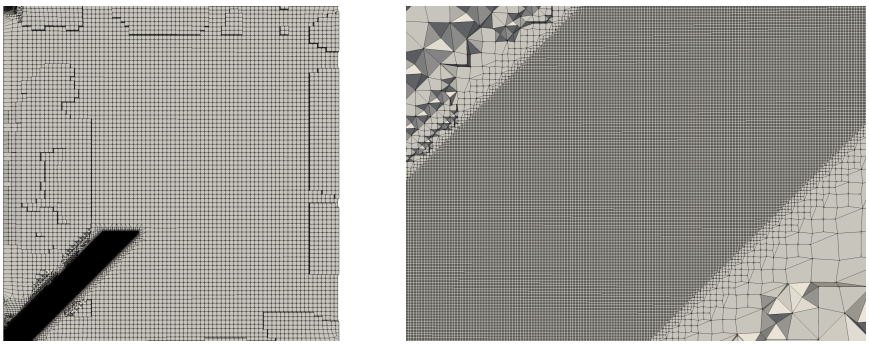

FIG. 14: Slice on the external mesh. Left: full mesh slice; right: refinement zone detail.

the external computational domain, several levels of decreasing refinment are used so that the total computational cost remains limited.

5.2 Coupling methodology

The coupling between the internal flow simulation and the external sectorial simulation is achieved by storing data for the velocity (**u**) and liquid volume fraction (α) from the internal flow simulation, at the plane that corresponds to the inlet boundary of the sector simulation (Section 4). The inlet boundary condition of the external flow simulation is applied through the *timeVaryingMappedFixedValue* boundary condition already implemented in *OpenFOAM*. This boundary condition takes the data from one field and linearly interpolates both in time and space, if needed. Data from the internal simulation were stored every $0.05\mu s$, which was checked to be sufficient to capture the essential features of the flow, in particular the air core rotation period.

In order to validate the efficiency of the boundary condition linking both simulations, it was checked if the swirl number and the turbulent kinetic energy was preserved among simulations. This study was done with the medium mesh of the internal flow simulation, for ambient operating conditions and with the WALE sub-grid scale model, as stated in Section 4.

5.2.1 Swirl number

The swirl number relates the swirling momentum to the axial motion. It was originally proposed by (Chigier and Beér, 1964) and later simplified by (Sheen et al., 1996), as follows:

$$SN = \frac{G_{tg}}{R\,G_{ax}} = \frac{\int_0^R wur^2 dr}{R\int_0^R u^2 r dr} \tag{11}$$

where SN is the swirl number, G_{tg} is the axial flux of the tangential momentum, G_{ax} is the axial flux of the axial momentum, R is the outer radius, and w and u are the tangential and axial velocity components at the corresponding radial position r, respectively.

Figure 15 shows the swirl number evolution along the axial axis (Z) for both the internal and external flow simulations. It can be appreciated that the input to the external flow simulation matches the output from the internal flow simulation, thus validating the data exchange among simulations after the interpolation process.

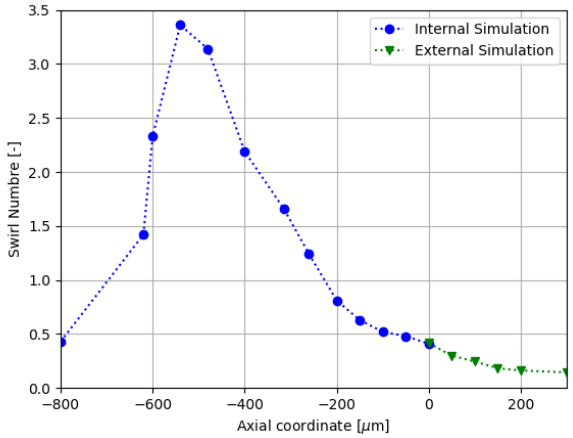

FIG. 15: Swirl number evolution along the axial axis for both the internal flow and external flow simulations.

5.2.2 Turbulent kinetic energy

The preservation of turbulent kinetic energy (*TKE*) during the mapping process is studied in this subsection. In order to assess the behavior of the method, the turbulent kinetic energy is plotted in Figure 16, where it is decomposed along each direction for both simulations involved.

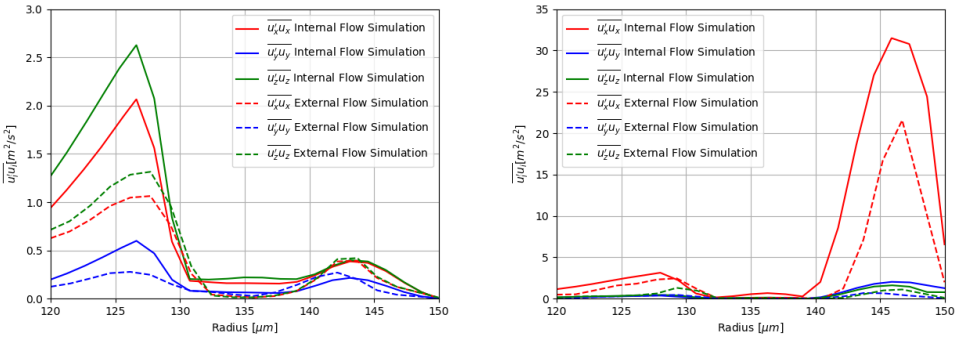

FIG. 16: Turbulent kinetic energy. Left: resolved scales; right: sub-grid energy.

It can be observed that, in general, a part of the turbulent kinetic energy is dissipated during the mapping procedure. This means that some features of the turbulent flow are lost during the mapping process, due to the required interpolation in space and time. Nevertheless, the main trends are preserved through the coupling procedure, ensuring a proper inlet condition for the external flow simulation. Still, the level of turbulent kinetic energy is underestimated at the inlet of the external flow simulation. In order to improve this point, a single simulation covering the whole computational domain is required, but as shown earlier this is beyond the scope of the present work.

5.3 Steady and unsteady fuel film thickness

In Section 4.6, it was shown that the amount of fuel sheet thickness fluctuations at the atomizer outlet depends on the chosen numerical schemes. With first order spatial schemes in the internal flow simulation, no fluctuations were recovered, but second order schemes provided fuel sheet instabilities. Two external flow simulations have been carried out mapping data at the inlet both with and without these instabilities coming from the internal flow simulation. Both external flow simulations are performed with second order discretization schemes in space and time, so as to isolate the role of the liquid film instabilities on primary breakup. Figure 17 shows the qualitative results obtained for these two cases. The iso-surface for $\alpha = 0.5$ is plotted for both cases and qualitatively compared with an experimental picture by (Miglierina, 2021).

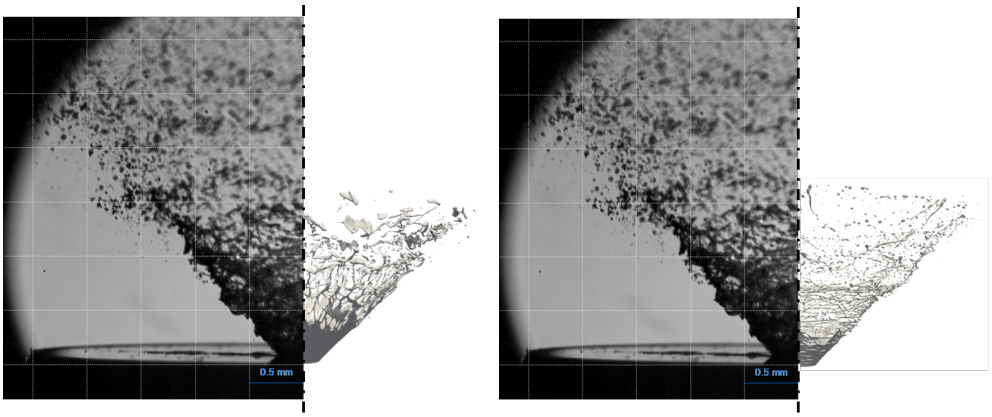

FIG. 17: Comparison of the liquid sheet atomization between experiment (shadowgraphy (Miglierina, 2021)) and numerical simulation (liquid-gas interface represented by the iso-surface $\alpha = 0.5$) for different data mapped at the inlet: constant liquid sheet thickness provided by first order schemes in the internal flow simulation (left), fluctuating liquid sheet thickness provided by second order schemes in the internal flow simulation (right).

It can be observed that the constant sheet thickness case (first order scheme used in the internal simulation to compute the mapped data) provides a liquid sheet surface that remains straight along the main flow direction until it breaks up, whereas the experiments show wrinkling or fluctuations of the liquid sheet starting from the nozzle orifice. Another observed difference concerns the arrangement of the ligaments that represent the intermediate state after liquid sheet perforation and before the breakup that shapes final droplets: in the experiments, the ligaments are arranged in a transversal direction (horizontal in the presented figure); in the numerical simulation, ligaments are shaped around perforations and then stretched, so they tend to aligned with the streamwise direction. Finally, the droplet formation does not seem to be fully developed, with most of the liquid elements being flat liquid structures. The predicted process of atomization is then similar to the breakup of a stretched liquid sheet Lohse and Villermaux (2020). It is worth mentioning that accurately capturing such a process would require an adaptation of the interface capturing method Chirco et al. (2022).

On the other hand, the results obtained by mapping the fuel injection with a fluctuating liquid film thickness (second order scheme used in the internal simulation to gather the mapped data) provide a better match with the experimental results. In this case, the liquid sheet starts fluctuating from the injector tip. Moreover, the ligaments are arranged in the same direction as

in the experiment, and the droplets are developed with sizes that qualitatively seem to be in the same order as the experimental ones.

This study points out that the liquid film thickness instability plays a driving role on the primary breakup mechanism of simplex pressure-swirl atomizers. Properly capturing these fluctuations is key to describing the atomization process. This was achieved in the current investigation thanks to a proper resolution of the internal flow. Consequently, an accurate modelling of the internal flow is essential and justifies the work devoted to the carefully measuring the internal geometry. In short, for this kind of atomizer it was found that the atomization process taking place outside the injector can be completely modified with a slight variation of the inner injection characteristics.

5.4 Further analysis

Figure 18 represents the liquid volume fraction α iso-contour ($\alpha = 0.5$) obtained through the external flow simulation. In order to obtain a view that more closely resembles the experimental results, the sectorial ($\varphi = 45°$) iso-surface has been copied and rotated to cover the 360° of the complete hollow cone, considering that a periodic boundary condition was used at the lateral regions of the external flow simulation.

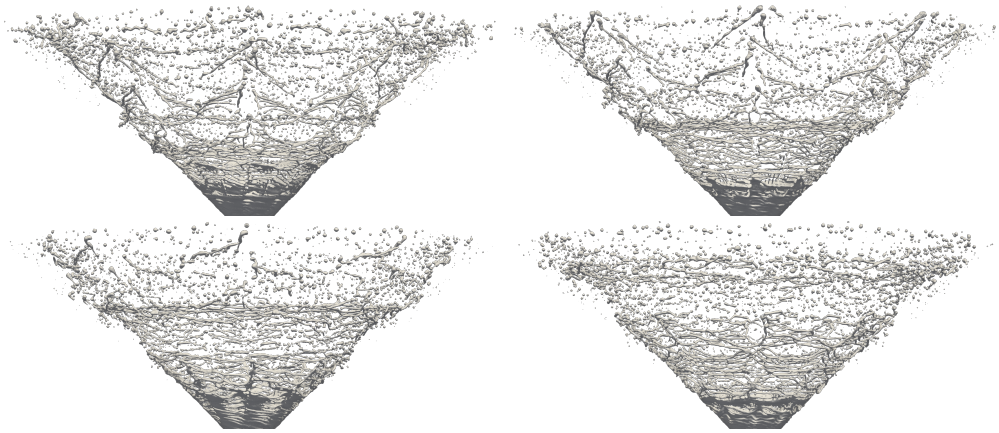

FIG. 18: Liquid volume fraction α contour ($\alpha = 0.5$) 360° render. From left to right, snapshots at: $t = 60\mu s$, $t = 65\mu s$, $t = 70\mu s$ and $t = 80\mu s$

A closer experimental view of the spray is compared to an instantaneous snapshot of the 3D rendering in Figure 19, including two different experimental pictures. At the left, the liquid volume fraction iso-surface is compared with the experiments by (Verdier et al., 2017). The arrangement of both experimental and predicted ligaments is similar, and it can be seen that the simulation yields drop sizes in the order of those from the experiments. At the right, numerical results are compared with a more recent experimental picture by (Miglierina, 2021), where a rearrangement of the experiment allow a better view right at the orifice outlet. In this experimental picture, it can be seen that small fluctuations on the fuel sheet are present right from the beginning, breaking it up near the nozzle orifice. This early breakup is captured by the numerical simulation. These comparisons show that there is a need for refined experimental data in order to properly characterise the early stage of the liquid sheet instability. Such experiments would allow going further in the comparisons with simulation data and constitute a topic of further

work. An additional feature commonly measured to characterize the atomization process is the drop size distribution. However, most experimental techniques (PDA, difraction, ...) require the existence of a disperse spray composed by spherical droplets. This means that such measurements are generally conducted further downstream of the atomizer outlet, where such conditions are achieved.

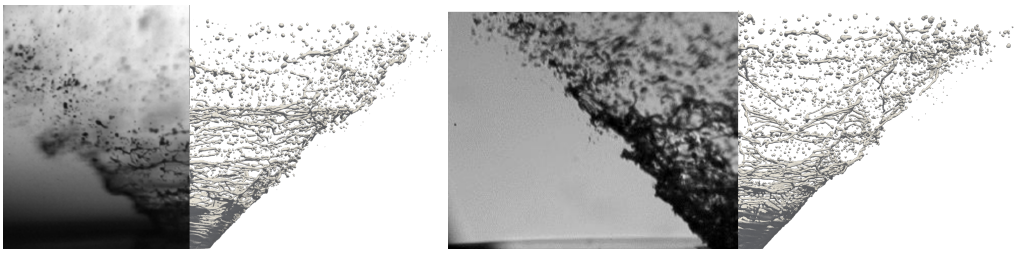

FIG. 19: Qualitative validation. Left: comparison with experiments by (Verdier et al., 2017); right: comparison with experiments by (Miglierina, 2021).

From a computational point of view, the drop size distribution can be determined applying the post-processing technique based on the surface interface Σ and the mean curvature κ proposed by (Palanti et al., 2022). A comparison between the drop size distribution extracted from the numerical modeling and those experimentally retrieved by PDA is shown in Figure 20. In the line of the previous statements, it must be noted that the numerical distribution is obtained at $Z = 1.2mm$, whereas experimental distributions are taken at $Z = 13mm$ (first downstream location where experimental PDA data was reported to be reliable by (Verdier et al., 2017)), and at two different radial positions: at the axis $R = 0mm$ and at an angle around 40° ($R = 10mm$).

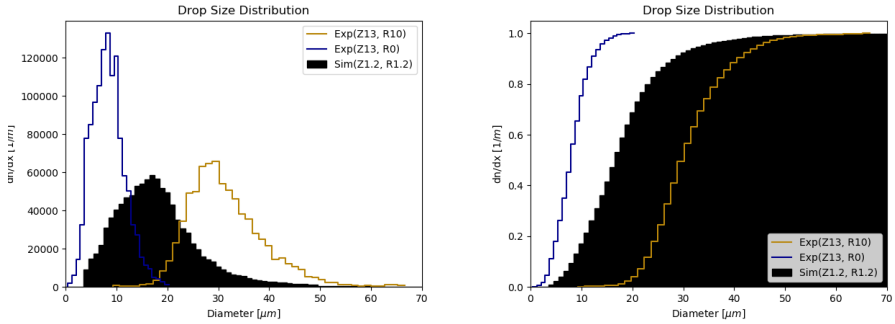

FIG. 20: Drop size distribution. Black Sim(Z1.2, R1.2): numerical results taken at $Z = 1.2mm$ and $R = 1.2mm$; blue line Exp(Z13, R0): experimental distribution placed at $Z = 13mm$ and $R = 0mm$; yellow line Exp(Z13, R10): experimental distribution placed at $Z = 13mm$ and $R = 10mm$. On the left: probability density function.On the right: cumulative distribution function.

Figure 20 shows that, near the axis, the experimental distribution (Exp(Z13,R0)) is mostly formed by small droplets ranging from $D = 1\mu m$ to $D = 20\mu m$ ($D_{32} = 12\mu m$). Meanwhile, the distribution taken at the spray cone angle (Exp(Z13,R10)) is wider and is formed by medium and big droplets in the $D = [10, 67]\mu m$ range ($D_{32} = 36\mu m$). This means that the smallest droplets tend to disperse into the hollow cone, whereas the largest ones remain in the streamwise direction thanks to their inertia. The distribution retrieved through the simulations is

obtained much closer to the orifice outlet, at the early stage of the atomization process. In order to reconstruct the drop size distribution, first, the curvature distribution is measured per unit of liquid surface. Then, the negative curvature (droplet curvatures are defined positive in this work) are filtered as they do not correspond to droplets and represent elements of surface not yet achieving an atomized status. Then, the diameter distribution is obtained from the definition of the curvature, assuming both main principal curvatures to be the same. This reconstruction finally requires one free parameter, which is set by enforcing the Sauter Mean Diameter obtained as the ratio of the liquid volume fraction to the liquid surface density. For more detail on the procedure to estimate the drop size distribution from the curvature distribution, please refer to (Palanti et al., 2022). Keeping in mind that the numerical drop size distribution is determined at a much earlier stage of the atomization process than the experimental one, the numerical drop size distribution ($D_{32} = 28\mu m$) falls between the two experimental distributions available. This is reasonable, since the departure in trajectories for the smaller droplets with respect to the larger droplets through the convection and dispersion processes has not been achieved yet in the numerical case. Thus, all the droplet are still collected by the post-processing technique applied in the numerical simulation.

6. CONCLUSION AND PERSPECTIVES

A complete analysis of a swirl injector representative of gas turbine injection and of interest for combustion research has been conducted. A workflow to replicate the process with any commercial injector has been defined, starting from the measurement of the internal geometry. Several measurement techniques such as computed tomography scan, optical microscope visualization and scanning electron microscope have been used to achieve an accurate description of the geometry. Both the actual metallic pieces and their silicon molds have been measured. The internal geometry has then been reconstructed and parametrized.

A two step coupling between numerical simulations has been proposed to separately study the internal flow of the injector and the external flow, focusing on the atomization process. A hybrid tetrahedral-hexahedral mesh is used on the internal flow simulation to avoid numerical instabilities due to the complexity of the geometry. The liquid volume fraction and velocity fields right at the orifice outlet were stored to feed the external flow simulation. In the latter, a full Cartesian mesh has been built to model the atomization process, where a high resolution zone is defined to properly capture separated liquid structures and the breakup process. It has been checked that both the swirl motion and the turbulence level are preserved between simulations. The predicted liquid-gas interface surface at the atomizer outlet shows a good qualitative agreement with experimental imaging, particularly if the liquid sheet fluctuations at the atomizer outlet found by the internal flow simulation are properly passed on to the external flow simulation.

Finally, the post-processing technique proposed by (Palanti et al., 2022) to reconstruct the drop size distribution based on the liquid surface and curvature analysis was applied to determine these metrics. Further investigations are needed both from the experimental and numerical standpoints to achieve a more final comparison, but the result obtained for the drop size distribution is compatible with reported experimental data.

The perspectives of this work are the combination of experimental and numerical studies to achieve synergies among them. Most experimental studies focus on the spray disperse phase, where the distribution and velocity of the droplets can be measured. However, the difficult optical access to certain zones, such as the internal part of the injector or even the first steps of the

atomization process, can be compensated through numerical simulation, providing instantaneous data on areas where the experiments can scarcely do so. The symbiosis of both methodologies could lead to improvements in both methodologies.

ACKNOWLEDGMENTS

Authors from Université de Rouen Normandie thankfully acknowledge the computer resources at IDRIS, TGCC and CINES under the allocation A0112B06153 and A0092B06153 made by GENCI (Grand Equipement National de Calcul Intensit) and also for the computing time at CRIANN (Centre Régional Informatique et d'Applications Numériques de Normandie) under the scientific project No. 2006011. This work has been possible thanks to the CHAIRLIFT European project 831881 - CHAiRLIFT - H2020-CS2-CFP08-2018-01.

Authors from Universitat Politècnica de València thankfully acknowledge the computer resources at Altamira (RES-IM-2020-1-0018) and MareNostrum (RES-IM-2020-412-0009) in the frame of the Spanish Supercomputing Network. Additionally, the support given to Dr. Marcos Carreres by "Ministerio de Educación, Cultura y Deporte" through the "Estancias de movilidad en el extranjero José Castillejo para jóvenes doctores" grant (ref. CAS18/00289) within the "Programa Estatal de Promoción del Talento y su Empleabilidad en I+D+i, Subprograma Estatal de Movilidad, del Plan Estatal de I+D+I" is gratefully acknowledged.

We would also like to thank Said Idlahcen, José Enrique del Rey and Ignacio Sevilla for their assistance with the experimental measurements of the atomizer geometry.

REFERENCES

Alajbegovic, A., Meister, G., Greif, D. and Basara, B., Three Phase Cavitating Flows in High-Pressure Swirl Injectors, *Experimental Thermal Fluid Science*, vol. **26**, pp. 677–681, 2002.

Amini, G., Liquid Flow in a Simplex Swirl Nozzle, *Int. J. Multiphase Flow*, vol. **79**, pp. 225–235, 2016.

Anez, J., Ahmed, A., Hecht, N., Duret, B., Reveillon, J. and Demoulin, F., Eulerian–Lagrangian Spray Atomization Model Coupled with Interface Capturing Method for Diesel Injectors, *Int. J. Multiphase Flow*, vol. **113**, pp. 325–342, 2019.

Boris, J. and Book, D., Flux-Corrected Transport. i. shasta, a Fluid Transport Algorithm that Works, *J. Computational Physics*, vol. **11**, no. 1, p. 38–69, 1968.

Chesnel, J., Reveillon, J., Menard, T. and Demoulin, F.X., Large Eddy Simulation of Liquid Jet Atomization, *Atomization Sprays*, vol. **21**, no. 9, pp. 711–736, 2011.

Chigier, N.A. and Bee´r, J.M., Velocity and Static-Pressure Distributions in Swirling Air Jets Issuing from Annular and Divergent Nozzles, *J. Basic Eng.*, vol. **86**, no. 4, pp. 788–796, 1964.

Chinn, J.J., An Appraisal of Swirl Atomizer Inviscid Flow Analysis, Part 2: Inviscid Spray Cone Angle Analysis and Comparison of Inviscid Methods with Experimental Results for Discharge Coefficient, Air Core Radius, and Spray Cone Angle, *Atomization Sprays*, vol. **19**, no. 3, pp. 283–308, 2009.

Chirco, L., Maarek, J., Popinet, S. and Zaleski, S., Manifold Death: A Volume of Fluid Implementation of Controlled Topological Changes in Thin Sheets by the Signature Method, *J. Computational Physics*, vol. **467**, p. 111468, 2022. URL https://www.sciencedirect.com/science/article/pii/S0021999122005307

Crank, J. and Nicolson, P., A Practical Method for Numerical Evaluation of Solutions of

Partial Differential Equations of the Heat-Conduction Type, *Mathematical Proceedings Cambridge Philosophical Society*, vol. **43**, no. 1, pp. 50–67, 1947.

Dafsari, R.A., Lee, H.J., Han, J., Park, D.C. and Lee, J., Viscosity Effect on the Pressure Swirl Atomization of an Alternative Aviation Fuel, *Fuel*, vol. **240**, pp. 179–191, 2019. URL https://doi.org/10.1016/j.fuel.2018.11.132

Ding, J.W., Li, G.X., Yu, Y.S. and Li, H.M., Numerical Investigation on Primary Atomization Mechanim of Hollow Cone Swirling Sprays, *Int. J. Rotating Machinery*, vol. **2016**, p. 11, 2016.

Durdina, L., Jedelsky, J., and Jicha, M., Investigation and Comparison of Spray Characteristics of Pressure- Swirl Atomizers for a Small-Sized Aircraft Turbine Engine, *Int. J. Heat Mass Transf.*, vol. **78**, pp. 892–900, 2014. URL http://dx.doi.org/10.1016/j.ijheatmasstransfer.2014.07.066

European Commission, E., Communication from the Commission to the European Parliament, the Council, the European Economic and Social Committee and the Committee of the Regions: Sustainable and Smart Mobility Strategy - putting European transport on track for the future, Tech. rep., European Commission, Brussels, 2020.

Fuster, D., Bague´, A., Boeck, T., Le Moyne, L., Leboissetier, A., Popinet, S., Ray, P., Scardovelli, R. and Zaleski, S., Simulation of Primary Atomization with an Octree Adaptive Mesh Refinement and VOF Method, *Int. J. Multiphase Flow*, vol. **35**, no. 6, pp. 550–565, 2009. URL https://linkinghub.elsevier.com/retrieve/pii/S0301932209000305

Galbiati, C., Tonini, S., Weigand, B. and Cossali, G.E., Direct Numerical Simulation of Primary Break-Up in Swirling Liquid Jets, *9th International Conference on Multiphase Flow*, Firenze, Italy, 2016.

Giffen, E. and Muraszew, A., *The Atomisation of Liquid Fuels*, Chapman Hall, 1953.

Hansen, K., Madsen, J., Trinh, C., Ibsen, C., Solberg, T. and Hjertager, B., A Computational and

Experimental Study of the Internal Flow in a Scaled Pressure-Swirl Atomizer, *ILASS-Europe 2002*, Zaragoza, Spain, 2002.

Jedelsky, J., Maly, M., Pinto del Corral, N., Wigley, G., Janackova, L. and Jicha, M., Air–Liquid Interactions in a Pressure-Swirl Spray, *Int. J. Heat Mass Transf.*, vol. **121**, pp. 788–804, 2018. URL https://doi.org/10.1016/j.ijheatmasstransfer.2018.01.003

Kim, S., Khil, T., Kim, D. and Yoon, Y., Effect of Geometric Parameters on the Liquid Film Thickness and Air Core Formation in a Swirl Injector, *Measurement Science Technology*, vol. **21**, no. 3, p. 015403, 2010.

Laurila, E., Koivisto, S., Kankkunen, A., Saari, K., Maakala, V., Ja¨rvinen, M. and Vuorinen, V., Computational and Experimental Investigation of a Swirl Nozzle for Viscous Fluids, *Int. J. Multiphase Flow*, vol. **128**, 2020.

Laurila, E., Roenby, J., Maakala, V., Peltonen, P., Kahila, H. and Vuorinen, V., Analysis of Viscous Fluid Flow in a Pressure-Swirl Atomizer using Large-Eddy Simulation, *Int. J. Multiphase Flow*, vol. **113**, pp. 371–388, 2019. URL https://doi.org/10.1016/j.ijmultiphaseflow.2018.10.008

Leask, S.B., Li, A.K., McDonell, V.G. and Samuelsen, S., Preliminary Development of a Measurement Reference using a Research Simplex Atomizer, *J. Fluids Eng., Transactions ASME*, vol. **141**, no. 12, pp. 1–11, 2019.

Lefebvre, A. and Suyari, M., Film Thickness Measurements in a Simplex Swirl Atomizer, *J. Propuls. Power*, vol. **2**, no. 6, p. 528–533, 1986.

Lefebvre, A.H. and Ballal, D.R., *Gas Turbine Combustion: Alternative Fuels and Emissions*, 3rd Edition, Boca Raton, FL: CRC Press, 2010.

Lefebvre, A.H. and McDonell, V.G., *Atomization and Sprays*, 2nd Edition, Boca Raton, FL: CRC Press, 2017.

Liu, C., Liu, F., Yang, J., Mu, Y., Hu, C. and Xu, G., Experimental Investigations of Spray Generated by a Pressure Swirl Atomizer, *J. Energy Institute*, vol. **92**, no. 2, pp. 210–221, 2019. URL https://doi.org/10.1016/j.joei.2018.01.014

Lohse, D. and Villermaux, E., Double Threshold Behavior for Breakup of Liquid Sheets, *Proceedings National Academy Sciences*, vol. **117**, no. 32, pp. 18912–18914, 2020. URL https://www.pnas.org/doi/abs/10.1073/pnas.2011358117

Macian, V., Bermu´dez, V., Payri, R. and Gimeno, J., New Technique for Determination of Internal Geometry of a Diesel Nozzle with the Use of Silicone Methodology, *Experimental Techniques*, vol. **27**, no. 2, pp. 39–43, 2003. URL http://doi.wiley.com/10.1111/j.1747-1567.2003.tb00107.x

Madsen, J., Hjertager, B., and Solberg, T., Numerical Simulation of Internal Flow in a Large-Scale Pressure- Swirl Atomizer, *ILASS-Europe 2004*, Nottingham, UK, pp. 183–188, 2004. URL http://citeseerx.ist.psu.edu/viewdoc/download?doi=10.1.1.131.9942& rep=rep1&type=pdf

Maly, M., Jedelsky, J., Slama, J., Janackova, L., Sapik, M., Wigley, G. and Jicha, M., Internal Flow and Air Core Dynamics in Simplex and Spill-Return Pressure-Swirl Atomizers, *Int. J. Heat Mass Transf.*, vol. **123**, pp. 805–814, 2018. URL https://doi.org/10.1016/j.ijheatmasstransfer.2018.02.090

Maly, M., Sapik, M., Cejpek, O., Wigley, G., Katolicky, J. and Jedelsky, J., Effect of Spill Orifice Geometry on Spray and Control Characteristics of Spill-Return Pressure-Swirl Atomizers, *Experimental Thermal Fluid Science*, vol. **106**, no. April, pp. 159–170, 2019. URL https://doi.org/10.1016/j.expthermflusci.2019.04.014

Miglierina, L., Liquid Injection for Gas Turbine, Master's thesis, Universite´ de Rouen Normandie, France, 2021.

Mongia, H., TAPS: A Fourth Generation Propulsion Combustor Technology for Low Emissions, *AIAA International Air and Space Symposium and Exposition: The Next 100 Years*, no. July, American Institute of Aeronautics and Astronautics, Reston, Virigina, pp. 1–11, 2003. URL https://arc.aiaa.org/doi/10.2514/6.2003-2657

Mulla, I.A., Godard, G., Cabot, G., Grisch, F. and Renou, B., Quantitative Imaging of Nitric Oxide Concentration in a Turbulent N-Heptane Spray Flame, *Combustion Flame*, vol. **203**, pp. 217–229, 2019a. URL https://doi.org/10.1016/j.combustflame.2019.02.005

Mulla, I.A., Godard, G., and Renou, B., Instantaneous Planar Measurements of Nitric Oxide Concentration in a Turbulent N-Heptane Spray Flame, *Combustion Flame*, vol. **208**, pp. 451–471, 2019b.

Mulla, I.A. and Renou, B., Simultaneous Imaging of Soot Volume Fraction, PAH, and OH in a Turbulent N-Heptane Spray Flame, *Combustion Flame*, vol. **209**, pp. 452–466, 2019. URL https://doi.org/10.1016/j.combustflame.2019.08.012

Nicoud, F. and Ducros, F., Subgrid-Scale Stress Modelling Based on the Square of the Velocity Gradient Tensor, *Flow, Turbulence Combustion*, vol. **62**, no. 3, pp. 183–200, 1999. URL https://doi.org/10.1023/A:1009995426001

Nural, O.E. and O¨ zgu¨r Ertunc¸, Predicting the Performance of Pressure-Swirl Atomizer, *Atomization Sprays*, vol. **28**, no. 6, p. 481–546, 2018.

Palanti, L., Puggelli, S., Langone, L., Andreini, A., Reveillon, J., Duret, B. and Demoulin, F.X., An Attempt to Predict Spray Characteristics at Early Stage of the Atomization Process by using Surface Density and Curvature Distribution, *Int. J. Multiphase Flow*, vol. **147**, p. 103879, 2022.

Park, B.S., Kim, H.Y., and Yoon, S.S., Transitional Instability of a Pressure-Swirl Atomizer due to Air-Core Eruption at Low Temperature, *Atomization Sprays*, vol. **17**, no. 6, pp. 551–568,

2007.

Rajamanickam, K. and Basu, S., Insights into the Dynamics of Spray–Swirl Interactions, *J. Fluid Mechanics*, vol. **810**, pp. 82–126, 2016.

Razeghi, A. and Ertunc¸, O¨., Numerical Investigation of Multiphase Flow Inside a Pressure Swirl Atomizer at the Initial Stage of Injection, *Atomization Sprays*, vol. **28**, no. 5, pp. 417–441, 2018.

Rizk, N. and Lefebvre, A., Internal Flow Characteristics of Simplex Swirl Atomizers, *J. Propuls. Power*, vol. **1,** no. 3, p. 193–199, 1985.

Rusche, H., Computational Fluid Dynamics of Dispersed Two-Phase Flows at High Phase Fractions, 2002.

Salvador, F.J., Gimeno, J., De la Morena, J. and Carreres, M., Comparison of Different Techniques for Characterizing the Diesel Injector Internal Dimensions, *Experimental Techniques*, vol. **42**, no. 5, pp. 467–472, 2018. URL http://link.springer.com/10.1007/s40799-018-0246-1

Scardovelli, R. and Zaleski, S., Direct Numerical Simulation of Free-Surface and Iitnerfacial Flow, *Annual Review Fluid Mechanics*, vol. **31**, pp. 567–603, 1999.

Shao, C., Luo, K., Yang, Y. and Fan, J., Detailed Numerical Simulation of Swirling Primary Atomization using a Mass Conservative Level Set Method, *Int. J. Multiphase Flow*, vol. **89**, pp. 57– 68, 2017.

Sheen, H.J., Chen, W.J., Jeng, S.Y. and Huang, T.L., Correlation of Swirl Number for a Radial-Type Swirl Generator, *Experimental Thermal Fluid Science*, vol. **12,** no. 4, pp. 444–451, 1996.

Shum-Kivan, F., Marrero Santiago, J., Verdier, A., Riber, E., Renou, B., Cabot, G. and Cuenot, B., Experimental and Numerical Analysis of a Turbulent Spray Flame Structure, *Proceedings Combustion Institute*, vol. **36**, no. 2, pp. 2567–2575, 2017.

URL http://dx.doi.org/10.1016/j.proci.2016.06.039

Simmons, H. and Harding, C., Some Effects of using Water as a Test Fluid in Fuel Nozzle Spray Analysis, *ASME. J. Eng. Power*, vol. **103,** no. 1, p. 118–123, 1981.

Som, S.K., Air Core in Pressure Swirl Atomizing Nozzles, *Atomization Sprays*, vol. **22**, no. 4, pp. 283– 303, 2012.

Sumer, B., Erkan, N., Uzol, O. and Tuncer, I.H., Experimental and Numerical Investigation of a Pressure Swirl Atomizer, *ICLASS 2012, 12th Triennial International Conference on Liquid Atomization and Spray Systems*, Heidelberg, Germany, 2012.

Sweby, P.K., High Resolution Schemes using Flux Limiters for Hyperbolic Conservations Laws, *Journal Numeric Analysis*, vol. **21,** no. 5, pp. 995–1011, 1984.

The OpenFoam Foundation, OpenFOAM 6, 2018. URL https://openfoam.org/version/6/

van Leer., B., Towards the Ultimate Conservative Difference Scheme. ii. Monotonicity and Conservation Combined in a Second-Order Scheme, *J. Computational Physics*, vol. **14,** no. 4, pp. 361–370, 1974.

Verdier, A., Marrero Santiago, J., Vandel, A., Saengkaew, S., Cabot, G., Grehan, G. and Renou, B., Experimental Study of Local Flame Structures and Fuel Droplet Properties of a Spray Jet Flame, *Proceedings Combustion Institute*, vol. **36**, no. 2, pp. 2595–2602, 2017.

Wardle, K.E. and Weller, H.G., Hybrid Multiphase Cfd Solver for Coupled Dispersed/Segregated Flows in Liquid-Liquid Extraction, *Int. J. Chemical Eng.*, vol. **2013**, p. 11, 2013.